Why Are There Rossby Wave Maxima in the Pacific at 10°S and 13°N?

ANTONIETTA CAPOTONDI AND MICHAEL A. ALEXANDER

NOAA–CIRES Climate Diagnostics Center, Boulder, Colorado

CLARA DESER

National Center for Atmospheric Research, Boulder, Colorado

(Manuscript received 23 January 2002, in final form 4 February 2003)

ABSTRACT

Observations indicate the existence of two bands of maximum thermocline depth variability centered at ~10°S and 13°N in the tropical Pacific Ocean. The analysis of a numerical integration performed with the National Center for Atmospheric Research ocean general circulation model (OGCM) forced with observed fluxes of momentum, heat, and freshwater over the period from 1958 to 1997 reveals that the tropical centers of thermocline variability at 10°S and 13°N are associated with first-mode baroclinic Rossby waves forced by anomalous Ekman pumping. In this study the factors that may be responsible for the Rossby wave maxima at 10°S and 13°N, including the amplitude and spatial coherency of the forcing at those latitudes, are systematically investigated. A simple Rossby wave model is used to interpret the OGCM variability and to help to discriminate between the different factors that may produce the tropical maxima. These results indicate that the dominant factor in producing the maximum variability at 10°S and 13°N is the *zonal coherency* of the Ekman pumping, a characteristic of the forcing that becomes increasingly more pronounced at low frequencies, maximizing at timescales in the decadal range. Local maxima in the *amplitude* of the forcing, while not explaining the origin of the centers of variability at 10°S and 13°N, appear to affect the sharpness of the variability maxima at low frequencies. Although the Rossby wave model gives an excellent fit to the OGCM, some discrepancies exist: the amplitude of the thermocline variance is generally underestimated by the simple model, and the variability along 13°N is westward intensified in the wave model but reaches a maximum in the central part of the basin in the OGCM. Short Rossby waves excited by small-scale Ekman pumping features, or the presence of higher-order Rossby wave modes may be responsible for the differences in the zonal variance distribution along 13°N.

1. Introduction

Thermocline processes have recently received considerable attention because of their potential role in climate variability at decadal timescales. Thermal anomalies have been observed to propagate along isopycnals from the surface midlatitudes toward the Tropics (Deser et al. 1996; Schneider et al. 1999) with a transit time of 7–8 yr. According to a recent theory of decadal climate variability (Gu and Philander 1997), the thermocline anomalies may reach the equator, where they have the potential to alter the upper ocean heat budget and give rise to equatorial sea surface temperature (SST) anomalies that may affect the atmosphere.

Another mechanism that can produce thermocline variability is propagation of baroclinic Rossby waves. Several midlatitude theories of decadal variability rely upon Rossby wave dynamics. Some of the proposed mechanisms (Latif and Barnett 1994, 1996; Robertson 1996; Jin 1997; Xu et al. 1998; Münnich et al. 1998; Grötzner et al. 1998; Talley 1999; Neelin and Weng 1999; Cessi 2000; Watanabe and Kimoto 2000) involve coupled ocean–atmosphere interactions, where changes in the surface wind stress induce changes in the strength of the subtropical gyre and in the northward heat transport by the western boundary current. These theories then postulate that the resulting sea surface temperature (SST) anomalies may affect the atmospheric circulation and ultimately produce changes in the surface wind stress. Since atmospheric processes are relatively fast, it is the slow oceanic adjustment that is responsible for the decadal timescales.

Although feedbacks of SST anomalies on the atmosphere can enhance the decadal signal, stochastic atmospheric forcing with a coherent basinwide spatial structure can also give rise to variability at interdecadal timescales (Jin 1997; Frankignoul et al. 1997; Neelin and Weng 1999). Frankignoul et al. (1997) have shown that a simple baroclinic Rossby wave model forced by a zonally uniform and temporally stochastic wind stress curl can produce spectra of the oceanic response that have enhanced power at low frequencies. The spectra

Corresponding author address: Antonietta Capotondi, NOAA–CIRES Climate Diagnostics Center, 325 Broadway, Boulder, CO 80305. E-mail: mac@cdc.noaa.gov

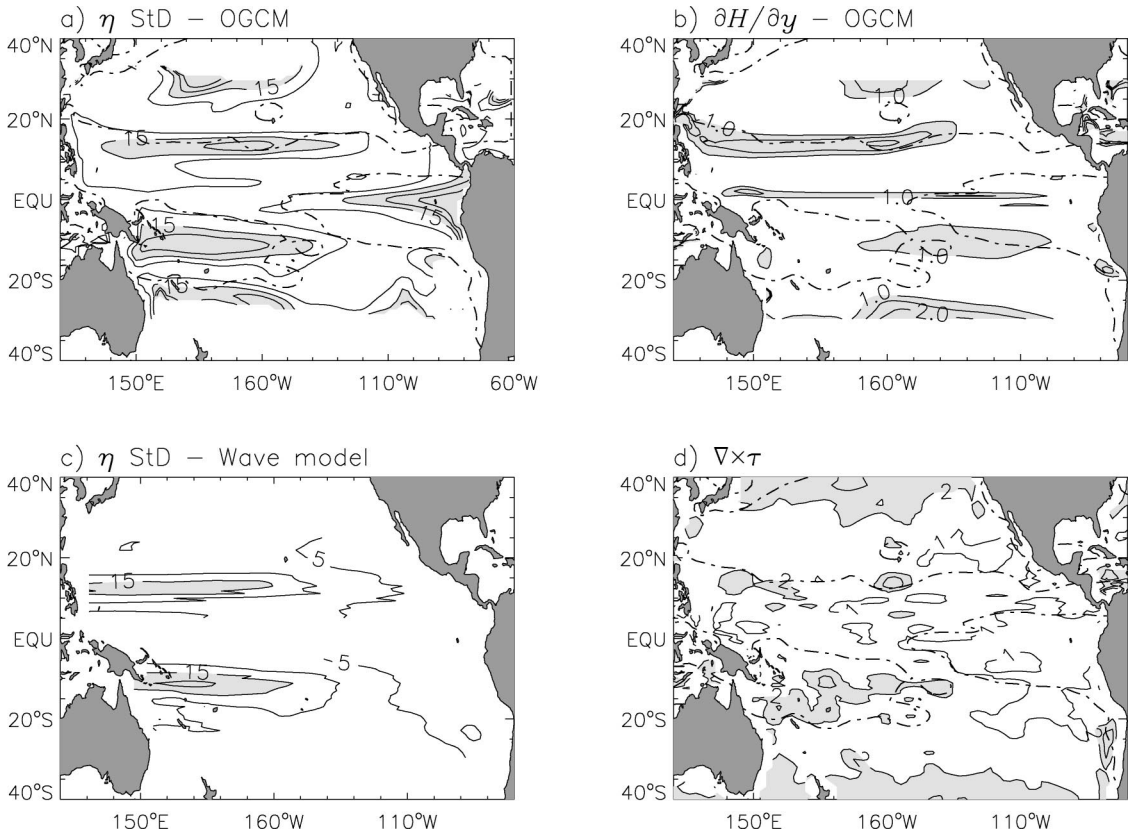

FIG. 1. (a) Standard deviation of the depth of the 25.5-σ_θ isopycnal diagnosed from a numerical simulation performed with the NCAR OGCM forced with observed fluxes of momentum, heat, and freshwater over the period 1958–97. Standard deviations are based upon 3-month averages of monthly anomalies (seasonal cycle removed). Contour interval is 5 m. Values larger than 15 m are shaded. (b) Meridional gradients of the depth of the 25.5-σ_θ isopycnal. Contour interval is 0.5×10^{-4}. Values larger than 10^{-4} are shaded. (c) Standard deviation of thermocline depth computed with the wave model forced by the same Ekman pumping field used to force the OGCM. Contour interval is 5 m. Values larger than 15 m are shaded. (d) Standard deviation of $\nabla \times \tau$, based on annual values. Contour interval is 1×10^{-5} cm s^{-1}. Values larger than 2×10^{-5} cm s^{-1} are shaded. The dot–dash line in (a), (b), and (d) is the line where the annual mean $\nabla \times \tau$ vanishes.

of the oceanic response predicted by the simple model vary spatially and at low frequencies become relatively more energetic in the western side of the basin.

The fundamental role of wind variability in forcing baroclinic Rossby waves has emerged in several observational and modeling studies (Kessler 1990 and references therein; Qiu et al. 1997). However, it is still unclear which aspects of the forcing are the most effective in exciting the oceanic baroclinic Rossby wave field, and how the influence of the wind forcing varies geographically. Is a spatially coherent and temporally stochastic forcing, as hypothesized by Frankignoul et al. (1997), sufficient to explain the energy level and spectral characteristics of the Rossby wave field over most of the ocean, or are additional aspects of the wind forcing important for the excitation of oceanic Rossby waves in some regions?

In the Pacific, thermocline variability is maximized in five areas, as shown in Fig. 1a. The standard deviation of the depth of the 25.5-σ_θ isopycnal, an isopycnal that lies in the core of the main thermocline, is used as a proxy for thermocline variability. Figure 1a is computed from an ocean general circulation model (OGCM) forced with observed fluxes of momentum, heat, and freshwater over the period from 1958 to 1997. A similar pattern of variability is found in observations (Lysne and Deser 2002). Two of the five centers of variability are found in the northern and southern midlatitudes, extending equatorward from the outcrop line of the 25.5-σ_θ isopycnal. Some fraction of these signals is likely associated with thermal anomalies subducting at the surface in midlatitudes and propagating equatorward within the main thermocline. A third area of large variability is found in the eastern equatorial Pacific and is associated with the El Niño–Southern Oscillation (ENSO). While the nature of the variability in midlatitudes and along the eastern equatorial Pacific is relatively well understood, the processes contributing to the two tropical centers of variability are in need of further investigation.

The two tropical centers lie approximately along the equatorward edges of the subtropical gyres in both

hemispheres, as indicated by the contours of zero wind stress curl in Fig. 1a. Since the wind stress curl changes sign at the gyre boundaries, displacements of the gyre structure can easily give rise to enhanced wind stress curl variability in these areas. Lysne and Deser (2002) have indeed found evidence of local maxima in wind stress curl variance at approximately 10°S and 13°N, as shown in Fig. 1d, and have suggested that the larger amplitude of the surface forcing in these areas may be the cause of the enhanced oceanic response.

Based on the analysis of the OGCM in Fig. 1a, Capotondi and Alexander (2001a, hereinafter CAa) have shown that the thermocline variability at 13°N consists primarily of first-mode baroclinic Rossby waves forced by anomalous Ekman pumping, and characterized by a large fraction of energy at periods longer than ~7 yr. At decadal periods (~7–10 yr), Ekman pumping anomalies east of the date line appear to propagate westward with a phase speed that is close to the phase speed of free Rossby waves, an aspect of the forcing which may be responsible for a preferred oceanic response at low frequencies. However, how relevant the westward propagation of Ekman pumping anomalies may be for explaining the center of variability at 13°N is still unclear.

The two tropical centers are also characterized by large meridional gradients of mean thermocline depth (Fig. 1b), and so meridional displacements of the isotherms could give rise to large thermal anomalies at a fixed latitude. It has long been known from observational studies (Wyrtki 1975; White 1977) that enhanced baroclinic variance tends to occur in areas of large horizontal gradients, with the implication that horizontal movements of the isotherms may produce local thermal anomalies. To our knowledge, the effectiveness of this process in producing variability maxima has never been verified. Capotondi and Alexander (2001b, hereinafter CAb) have provided estimates of meridional shifts of the isotherms at 13°N, and have shown that the displacements detected with their method can explain a large fraction of the temperature and depth variability in the thermocline between 10°–15°N, but it is not clear to what extent the meridional displacements are independent of the Rossby wave field itself.

In this paper we systematically examine the aspects of the surface forcing that may give rise to the centers of variability at 10°S and 13°N, and clarify their relative roles. Some specific questions are addressed. 1) Can the surface Ekman pumping produce the two tropical centers of variability? 2) If the answer to question 1 is positive, which aspect(s) of the forcing are the most important: amplitude, spatial/temporal coherency, or propagation characteristics? 3) Can the meridional excursions of the thermocline detected by CAb be a manifestation of the propagating Rossby waves? To answer these questions we analyze the OGCM simulation considered by CAa and CAb. A simple wave equation is also used to help interpret the OGCM results and discriminate between the different factors that may be responsible for the two tropical centers of variability.

The presentation of this study is organized as follows. In section 2 we describe the OGCM and the wave model. In section 3 the wave model is used to assess which aspects of the surface Ekman pumping are the most important in producing the large thermocline variability at 13°N and 10°S. In section 4 we discuss the origin of the large zonal coherency of the Ekman pumping along 10°S and 13°N, and whether meridional shifts of the isotherms can result from the Rossby wave field itself. We conclude in section 5.

2. The models

a. The OGCM

The OGCM used for this study is the National Center for Atmospheric Research (NCAR) ocean model (NCOM) that has been described in detail in Large et al. (1997, 2001) and Gent et al. (1998). In this section we only provide a brief summary of the basic model characteristics and information about the surface forcing used for the numerical simulation analyzed here.

NCOM is derived from the Geophysical Fluid Dynamics Laboratory (GFDL) Modular Ocean Model with the addition of a mesoscale eddy flux parameterization along isopycnal surfaces (Gent and McWilliams 1990) and a nonlocal planetary boundary layer parameterization (Large et al. 1994). The model is global, with a horizontal resolution of 2.4° in longitude and varying resolution in latitude ranging from 0.6° near the equator to 1.2° at high latitudes. The model version used for this study includes an anisotropic viscosity parameterization (Large et al. 2001) with enhanced viscosity close to ocean boundaries and much weaker viscosity in the ocean interior.

The surface forcing includes momentum, heat, and freshwater fluxes for the period from 1958 to 1997. The wind stress is computed from the reanalyses fields produced at the National Centers for Environmental Prediction (NCEP; Kalnay et al. 1996) using bulk formulas. The sensible and latent heat fluxes are computed from the NCEP winds and relative humidity and the model's SSTs using standard air–sea transfer equations (Large and Pond 1982; Large et al. 1997). Sensible and latent heat fluxes depend on the difference between SST and surface air temperature. Since SST and air temperature closely track each other, when observed air temperatures are used in the bulk formulas, as in the present model simulation, the model's SST is relaxed toward observations (Haney 1971). The relaxation timescale is relatively short (30–60 days for typical mixed layer depths), and so the SST in the model can be expected to be strongly constrained by the surface forcing rather than by the interior ocean dynamics.

The numerical simulation is started from an initial condition obtained from a preliminary climatological

integration so that the initial model state is not too different from the mean state characteristic of the 40-yr experiment. Then the model was run for two 40-yr cycles, the second cycle starting from the conditions achieved at the end of the first 40-yr segment. The mismatch between the model state and the forcing at the beginning of the second cycle did not seem to produce any long-term transient. Here we analyze the output for the second 40-yr period using monthly and annual mean values. Some residual drift in temperature and salinity appears to be confined to depths larger than approximately 500 m (Doney et al. 2003).

b. The wave model

To interpret the OGCM results we consider a 1½-layer, reduced-gravity system, in which the upper ocean of density ρ_1 overlies an infinitely deep, motionless bottom layer of density ρ_2. Under the low-frequency, quasigeostrophic assumptions, and in the long wave limit, the equation for the upper-layer thickness η can be written in the form (Qiu et al. 1997):

$$\frac{\partial \eta}{\partial t} - c_r \frac{\partial \eta}{\partial x} = -W_E(x, t) - R\eta, \tag{1}$$

where $c_r = \beta\lambda^2$ is the phase speed of the long, free baroclinic Rossby waves, β is the meridional gradient of the Coriolis parameter, f, $\lambda = c/f$ is the baroclinic Rossby radius, $c = \sqrt{g'H}$ is the long gravity wave phase speed, $g' = g(\rho_2 - \rho_1)/\rho_o$ the reduced gravity, g the acceleration of gravity, ρ_o the mean ocean density, H the mean upper-layer depth, W_E the Ekman pumping defined as

$$W_E = \nabla \times \left(\frac{\tau}{\rho_o f}\right), \tag{2}$$

τ is the wind stress, and $-R\eta$ is a Rayleigh friction term. The Rayleigh frictional timescale, $1/R$, has been chosen to be 2 yr, based on a sensitivity analysis described by CAb. The Rossby radii of deformation have been estimated by CAa for the given model stratification using the Wentzel–Kramers–Brillouin (WKB) approximation (Morse and Feshbach 1953). Equation (1) describes the geostrophic motion below the surface Ekman layer, where the meridional transport V_g is dictated by the surface Ekman pumping:

$$V_g = \frac{f}{\beta} W_E. \tag{3}$$

Thus, Eq. (1) differs from the full Sverdrup model, which includes both geostrophic and Ekman transports, and where the total transport V is given by

$$V = \frac{\nabla \times \tau}{\beta}. \tag{4}$$

Equation (1) is solved at each latitude along Rossby wave characteristics:

$$\eta(x, t) = \eta(x_e, t - t_e)e^{-Rt_e} + \int_{x_e}^{x} \frac{W_E(\xi, t - t_\xi)}{c_r(\xi)} e^{-Rt_\xi}\, d\xi, \tag{5}$$

where the solution at each point x and time t is obtained as the superposition of the Rossby waves generated east of point x at previous times. The first term on the right hand side (rhs) of Eq. (5) is the contribution of the waves generated at the eastern boundary x_e and reaching point x at time t with a transit time

$$t_e = \int_{x_e}^{x} \frac{d\xi}{c_r(\xi)}.$$

The second term on the rhs of Eq. (5) is the contribution of the waves generated by the Ekman pumping east of the target point x, with

$$t_\xi = \int_{\xi}^{x} \frac{d\varsigma}{c_r(\varsigma)}.$$

Both boundary and wind-forced terms decay while propagating westward with the frictional timescales $1/R$. CAa have shown that variations of thermocline depth at the boundary influence the interior solution only within 10°–20° from the boundary, while the largest signals away from the eastern boundary are due to the wind forcing, in agreement with observational studies (Kessler 1990). Thus, in seeking a solution to Eq. (1) we neglect the boundary contribution and focus upon the wind-driven component. As seen from Eq. (5), this component depends not only upon the magnitude of the integrand (W_E/c_r), but also upon the way the signals generated at different longitudes superimpose, which, in turn, may be related to the longitudinal coherency of the forcing. In section 3 we will examine the influence of these different aspects of the forcing in controlling the amplitude of the thermocline variability.

3. Wind forcing

As a first step, we assess how well the Rossby wave equation [Eq. (1)] can explain the thermocline variability in the Tropics. The wave equation is solved in the latitude band 25°S–25°N, with the exclusion of the area 5°S–5°N, and is forced with monthly anomalies of Ekman pumping from the NCEP–NCAR reanalyses, the same forcing used for the OGCM. The standard deviation of thermocline depth computed from the wave equation is shown in Fig. 1c. The two tropical centers of variability are present in the wave equation solution at approximately the same location and with comparable amplitude as in the OGCM. The detailed longitudinal structure of the variability at 13°N is somewhat different in the OGCM (Fig. 1a) as compared with the wave model (Fig. 1c) in that the variability in the wave model is westward intensified, while in the OGCM maximum amplitudes are found around 160°W.

The local temporal correlations between the solution

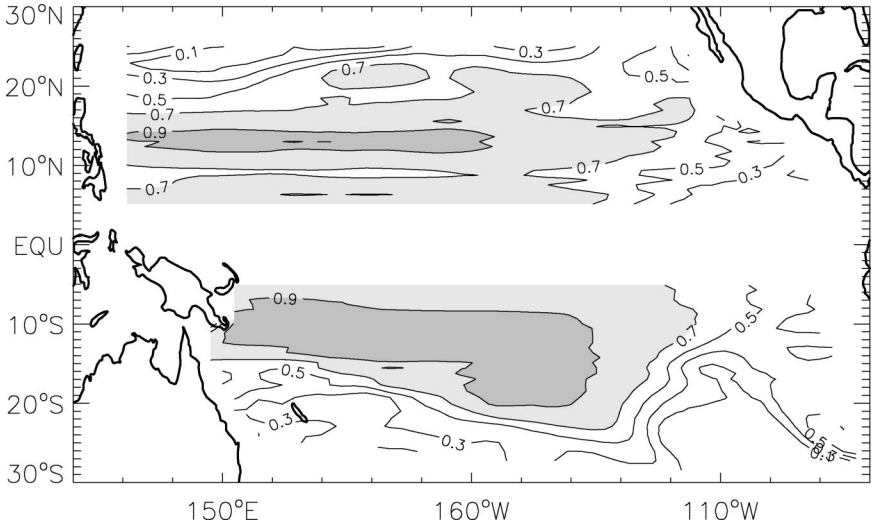

FIG. 2. Correlations between the thermocline depth variations computed from Eq. (1) forced with the observed W_E (Fig. 1c), and the depth variation of the 25.5-σ_θ isopycnal from the OGCM (Fig. 1a). Light shading indicates correlations larger than 0.7, while dark shading is used for correlations larger than 0.9.

of Eq. (1) and the variations of the 25.5-σ_θ isopycnal in the OGCM (Fig. 2) are larger than 0.7 between 18°S and 18°N, and west of approximately 120°W, with values larger than 0.9 around 10°S and 13°N, indicating that Eq. (1) is an excellent framework to describe the OGCM variability in the Tropics. The presence of the centers of variability around 10°S and 13°N in the solution to Eq. (1), as seen in the OGCM, is an indication that some aspects of the Ekman pumping can give rise to enhanced variability in those areas. In the following sections we examine which aspects of the forcing are the most relevant.

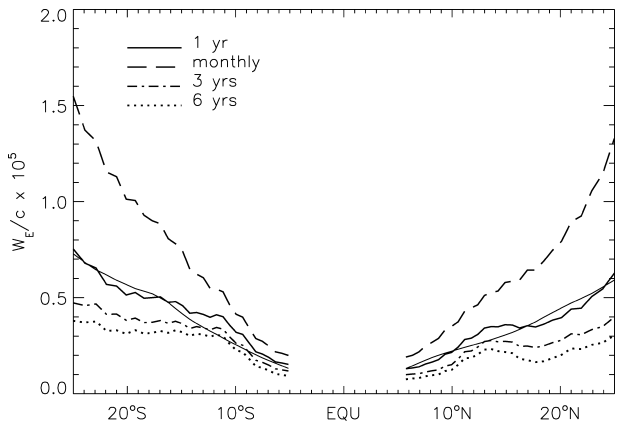

FIG. 3. Ratio of the zonally averaged standard deviation of W_E and the zonally averaged Rossby wave phase speed c_r as a function of latitude. The dashed line is obtained using monthly anomalies of the W_E field, the thick solid line is computed from 1-yr low-pass filtered values, the dot–dash line is from 3-yr low-pass filtered values, and the dot line is from 6-yr low-pass filtered values. The W_E values have been multiplied by 10^5. The thin solid line is obtained using the 1-yr low-pass filtered $\tilde{W}_E$ field, where the local maxima of fW_E are removed.

a. Amplitude of the forcing

We first examine whether the latitudinal dependence of the amplitude of the Ekman pumping can explain the presence of the two tropical maxima of thermocline variability. Lysne and Deser (2002) found local maxima in wind stress curl variability in those areas based on annual values (the standard deviation of the wind stress curl computed from monthly anomalies does not show any pronounced local maxima in the same regions). However, since we are interested only in the interior geostrophic flow, Ekman pumping [Eq. (2)], rather than wind stress curl ($\nabla \times \tau$) is the actual forcing term of the wave model Eq. (1). The integrand of the characteristics solution Eq. (5) is $W_E/c_r = V_g f/c^2$, indicating that meridional motions are a fundamental part of Rossby waves and that the latitudinal variations of the integrand depends not only upon the meridional variations of the Ekman pumping but also upon the variation of the phase speed with latitude.

Figure 3 shows the latitudinal dependence of the standard deviation of W_E, zonally averaged across the basin, divided by the zonally averaged phase speed. Monthly anomalies of W_E are considered, as well as 1-, 3-, and 6-yr low-pass filtered anomalies. The latitudinal variation of W_E/c_r depends upon the timescales of the Ekman pumping. When monthly anomalies are used, W_E/c_r increases monotonically with latitude, while small local maxima (or inflection points) are found at ~11°–12°S and 13°–15°N when timescales shorter than 1 yr are filtered out. The presence of these local maxima becomes relatively more pronounced at longer timescales, due to the decreased variance of the filtered W_E fields, but no absolute maximum of W_E/c_r is found in the Tropics.

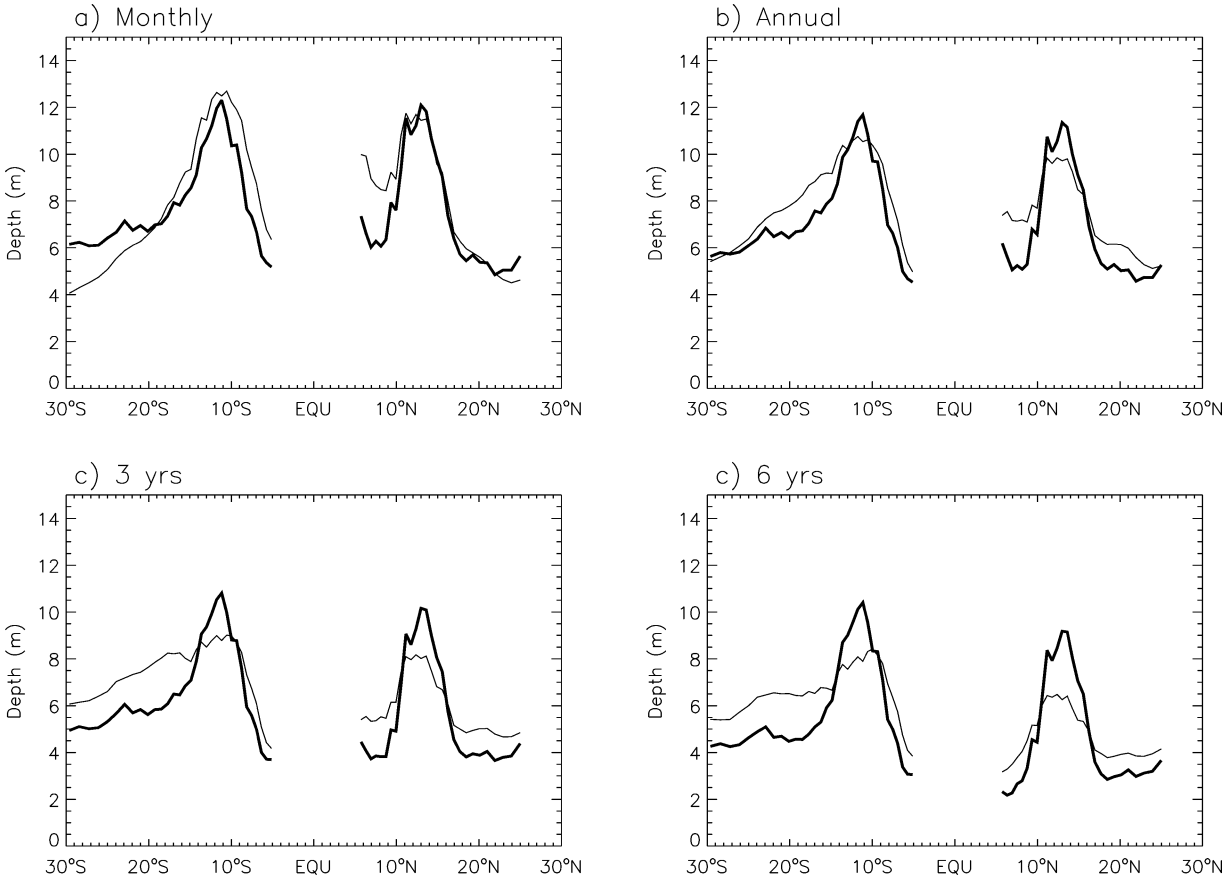

FIG. 4. (a) Comparison of the zonally averaged standard deviation of thermocline depth variations forced by the monthly anomalies of the observed W_E (thick line) and zonally averaged standard deviation forced by the corresponding $\tilde{W}_E$ field (thin line). (b) As in (a) but for 1-yr low-pass filtered W_E. (c) As in (a) but for a 3-yr low-pass filtered W_E. (d) As in (a) but for 6-yr low-pass filtered W_E.

The variance of W_E increases as $1/f$ with decreasing latitude [Eq. (2)], while the phase speed varies as $1/f^2$ so that W_E/c_r varies approximately as f. Thus, the latitudinal variation of the integrand in Eq. (5) can explain the decreasing amplitude of the solution equatorward of 10°S and 13°N, but it cannot explain the presence of the two maxima and the poleward decrease seen in Fig. 1c. The phase speed also varies with latitude because of changes in stratification, but this latter factor is found to be secondary to the f dependence of c_r (not shown).

To clarify the role of the local maxima of W_E/c_r at timescales of 1 yr and longer we solve Eq. (1) with modified W_E fields, $\tilde{W}_E$. Since poleward of ~10° W_E is very close to $\nabla \times \tau/f$ and the local maxima in W_E/c_r are likely associated with the maxima in $\nabla \times \tau$ (see Fig. 1d), the $\tilde{W}_E$ fields have been obtained by first normalizing the time series of fW_E at each grid point to unit standard deviation, and then multiplying it by the average standard deviation of fW_E over the areas (6°–25°N, 140°E–130°W) and (20°–6°S, 160°E–95°W) in the Northern and Southern Hemispheres, respectively. Thus, the standard deviation of $f\tilde{W}_E$ is spatially uniform, but close to the average standard deviation of fW_E, and $\tilde{W}_E$ varies with latitude as $1/f$. As an example, the latitudinal variation of $\tilde{W}_E/c_r$ for the 1-yr low-pass filtered anomalies is shown in Fig. 3 as a thin solid line. It captures the average variation of the annual W_E/c_r but its latitudinal dependence is purely monotonic.

In Fig. 4 the zonally averaged standard deviation of thermocline depth variations from the wave model forced with monthly, 1-, 3-, and 6-yr low-passed filtered W_E fields is compared with the η standard deviation obtained with the corresponding $\tilde{W}_E$ fields. At yearly and longer timescales (Figs. 4b–d), the $\tilde{W}_E$ fields produce tropical centers of variability that are broader and weaker than those obtained with W_E, characteristics that become progressively more pronounced at lower frequencies. These results indicate that the local maxima in W_E/c_r do affect the sharpness of the tropical centers of variability, but not their existence. Thus, the *amplitude* of the integrand in Eq. (5) cannot explain the presence of the maxima and, in particular, the amplitude decrease poleward of 10°S and 13°N. Figure 4 also shows that, despite the dramatic decrease of W_E/c_r when the Ekman pumping is low-pass filtered, the maximum thermocline variability at 10°S and 13°N remains quite large, indicating that the ocean model responds preferentially to the low frequencies of the forcing.

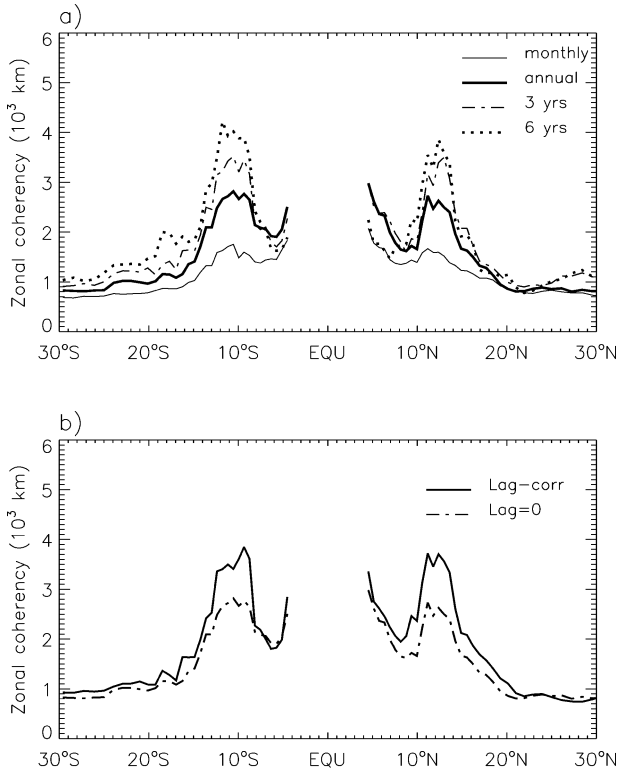

FIG. 5. (a) Zonally averaged coherencies of Ekman pumping anomalies based on monthly values (thin solid line), 1-yr low-pass filtered values (thick solid line), 3-yr low-pass filtered values (dot–dash line), and 6-yr low-pass filtered values (dot line). Instantaneous correlations are used. (b) Zonally averaged coherencies of 1-yr low-pass filtered Ekman pumping anomalies based on lag correlations (solid line) and instantaneous correlations (dot–dash line).

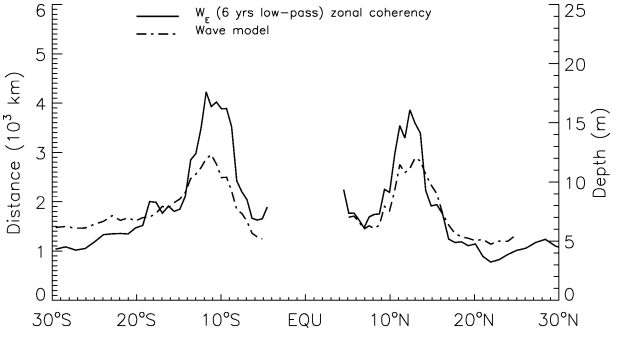

FIG. 6. Comparison between the zonally averaged coherency of W_E (thick solid line, left axis) based on instantaneous correlations of the 6-yr low-pass filtered values and the zonally averaged standard deviation of thermocline depth from the wave model (dot–dash line, right axis).

b. Spatial coherency

If the integrand in the second term of the Rossby wave solution in Eq. (5) cannot explain the maxima at 10°S and 13°N in Fig. 1c, then the zonal coherency of the forcing may be important. If, for example, the Ekman pumping time series at each longitude were completely uncorrelated in time, the resulting wave field would also be spatially incoherent. If, on the other hand, the Ekman pumping were coherent over a large distance, the waves generated at different points may superimpose constructively and give rise to a larger amplitude response. To test this hypothesis we compute zonal decorrelation length scales for the Ekman pumping. At each latitude, we consider the correlations between W_E at each grid point x and W_E at other points x' along the same latitude circle. Eastward and westward directions are considered independently. For each direction the decorrelation length is computed as the minimum distance at which correlations decrease to values lower than 0.5. Since we are interested in assessing maximum distances over which the forcing is coherent, the maximum of the eastward and westward values is chosen as the decorrelation length scale for W_E at the given point x. Because of the strong timescale dependence exhibited by W_E/c_r in section 3a, zonal coherencies are computed for monthly anomalies, as well as for 1-, 3-, and 6-yr low-pass filtered W_E fields.

At all timescales the zonal coherency of W_E is a maximum along 10°S and 13°N, where W_E is coherent across the eastern two-thirds of the basin (not shown). Since W_E is not defined close to the equator, the equatorial band has been excluded from the coherency computation. The tropical coherency maxima increase at longer timescales. When monthly W_E anomalies are considered, the maxima at 10°S and 13°N in Fig. 5a are barely noticeable but become more pronounced as the timescale increases. In particular, the zonal coherencies at 10°S and 13°N for the 6-yr low-pass filtered values are ~40% larger than the coherencies obtained with the 1-yr low-pass filtered field.

The zonal coherencies in Fig. 5a are based on instantaneous correlations. If lag correlations are instead used to estimate the zonal coherency of W_E, the maximum coherencies along 10°S and 13°N increase, when lags between −3 and 3 yr are considered (Fig. 5b). At 10°S and 13°N zonal coherencies are ~30% larger when lag correlations are used. The lag dependence of the zonal coherency at 10°S and 13°N indicates that there are zonal phase variations of the Ekman pumping along those latitudes. At 13°N phase variations can be attributed to the westward propagation of Ekman pumping anomalies described by CAa, who suggested that westward propagation may be responsible for a particularly efficient excitation of the Rossby wave field. The influence of the zonal phase variations upon the amplitude of the response along 13°N will be examined at the end of section 3c.

In Fig. 6 the zonal average of the decorrelation length based on instantaneous correlations of 6-yr low-pass filtered values is compared with the zonal average of the thermocline depth standard deviation computed from the simple wave model, as a function of latitude. The maxima in Rossby wave amplitude (thick dot–dash line) are closely aligned with the maxima in decorre-

lation length (thick solid line), supporting the hypothesis that the spatial coherency of the forcing is a key element in determining the amplitude of the resulting Rossby wave field.

c. Temporal coherency

The results of section 3b indicate that zonally coherent Ekman pumping anomalies may be central for the existence of the variability maxima along 10°S and 13°N. What about temporal coherency? Of course the two are not independent. In particular, we can expect that longer length scales are associated with longer timescales. Figure 5a confirms this hypothesis, by showing that spatial coherencies increase with decreasing frequencies, and in particular they are larger at timescales longer than the interannual ENSO timescales.

In section 3b we have also seen that there are zonal phase variations in the Ekman pumping field and that the inclusion of these phase differences can lead to larger decorrelation lengths. How important are these phase differences? At 13°N Ekman pumping anomalies are coherent approximately between 180° and 120°W. Within this longitudinal band, the Ekman pumping at the eastern edge of the coherent region appears to lead the Ekman pumping farther west. Lags tend to progressively increase westward (CAa), suggesting a westward propagation of the Ekman pumping anomalies. Using cospectral analysis, CAa have shown that the propagation is especially consistent at decadal timescales, and have estimated a westward phase speed for the decadal Ekman pumping anomalies of ~9 cm s^{-1}, a value that is comparable to the phase speed of the first mode baroclinic Rossby waves (~15 cm s^{-1}), and have suggested that this ''quasi resonance'' may play an important role in exciting a vigorous Rossby wave field. At 10°S, however, no indication of westward propagation is found (not shown). On the contrary, Ekman pumping in the eastern basin appears to lag the forcing farther west, consistent with eastward propagation, if any.

To clarify the role of temporal coherency and zonal phase variations, we randomly scramble the time series of the monthly Ekman pumping anomalies and create a new field W_E^{sc}. A sequence of random numbers is created using a ''Mersenne Twister'' algorithm (Matsumoto and Nishimura 1998) and that sequence is used at each grid point to alter the time series of monthly Ekman pumping anomalies. The same sequence of random numbers is used at each grid point so that time series at different locations are altered in a similar fashion. Thus, this procedure not only preserves the variance of the time series at each location, but instantaneous correlations between time series at different points are also preserved. However, lag correlations may be altered. Also, as we apply the scrambling procedure to monthly anomalies, the resulting fields can be expected to have a reduced low-frequency content, and increased energy at high frequencies. To increase the statistical significance of the results, an ensemble of 99 W_E^{sc} fields has been considered.

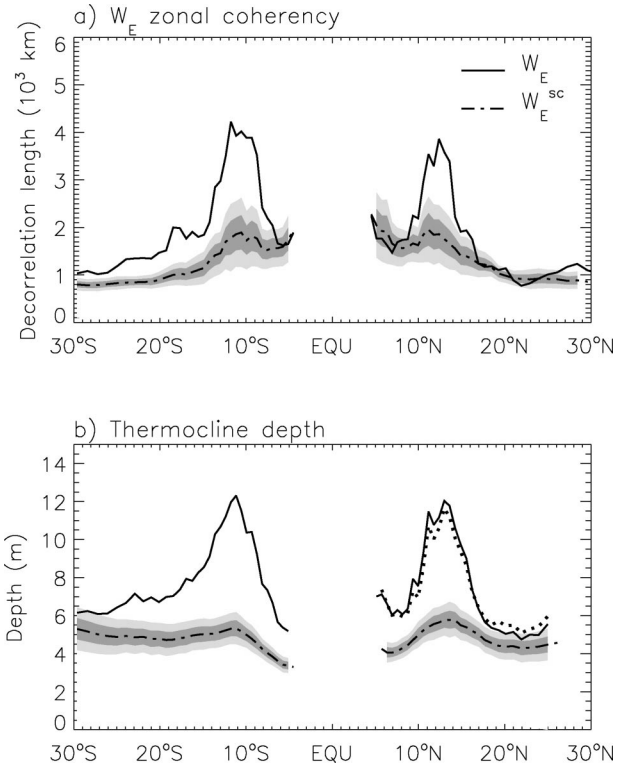

FIG. 7. (a) Comparison between the zonally averaged coherency of W_E (solid line), based on 6-yr low-pass filtered values, and the ensemble mean of the zonally averaged coherency of W_E^{sc} (dash–dot line). The ensemble contains 99 realizations of W_E^{sc}. Each W_E^{sc} field is obtained by randomly scrambling the monthly time series of W_E at each grid point. Decorrelation lengths were then calculated from the annually averaged scrambled time series. The dark shading indicates values of decorrelation lengths within 1 std dev from the ensemble mean, while the light shading shows values within 2 std dev from the ensemble mean. (b) Comparison between the zonally average standard deviation of thermocline depth obtained from the wave model forced by W_E and the ensemble mean of the zonally averaged standard deviation obtained with the W_E^{sc} fields. Values of thermocline depth standard deviation within 1 and 2 std dev from the ensemble mean are indicated by dark and light shading, respectively. The dot line in (b) shows the zonally averaged standard deviation of thermocline depth obtained with the modified forcing W_E^{sym} between 5° and 25°N.

Figure 7a compares the zonally averaged coherency of W_E, based on 6-yr low-pass filtered values, with the zonally averaged ensemble mean coherency of the W_E^{sc} fields, respectively. Values of W_E^{sc} zonal coherency within one and two standard deviations from the ensemble mean are also shown by the shaded areas. Although the zonal coherencies of W_E^{sc} still show maxima at 10°S and 13°N, their values are largely reduced. The ensemble averages at the location of the two tropical maxima are more than 50% smaller than the corresponding maxima of the original W_E field. The ensemble average coherency for the W_E^{sc} fields is very similar to the coherency obtained with monthly anomalies using

instantaneous correlations (Fig. 5a). As a consequence of the decreased zonal coherency, the amplitude of the thermocline variability excited by the W_E^{sc} fields is much smaller, as seen in Fig. 7b, where the zonally averaged thermocline depth standard deviation produced by the W_E^{sc} fields (in an ensemble average sense) is compared with the zonally averaged standard deviation forced by the original W_E field. When W_E^{sc} are used, the tropical maxima at 10°S and 13°N are much weaker, with amplitude reductions of the order of 50%, and a much less pronounced poleward decrease in amplitude.

The effect of the time scrambling procedure is twofold: first, phase relationships between the forcing at different points are altered at timescales greater than 1 month, and so any propagation feature can be expected to be severely distorted; and second, low-frequency energy is reduced and high-frequency energy increased, thus emphasizing smaller spatial scales.

To understand which of these two effects is the most important in producing the drastic reduction in thermocline variability observed with W_E^{sc} (Fig. 7b), we perform an additional experiment by forcing the wave model with another modified Ekman pumping field. In this case, the W_E values between 150° and 120°W are symmetrically exchanged with the values between 150°W and 180°. This procedure is applied north of 7.5°N since clearer indications of propagation were found at 13°N. The Ekman pumping is coherent approximately between the date line and 120°W, and in the same latitude band indications of westward propagation were found by CAa. By mirroring the values in the 150°W–180° longitude band with the values in the 150°–120°W band, spatial coherencies are left unaffected, but westward propagation becomes eastward propagation. The thermocline variability found with the new W_E field (W_E^{sym}) is very similar in amplitude to the variability found with the original W_E field (Fig. 7b), indicating that the westward propagation of the forcing and its quasi-resonance with the free Rossby waves at this latitude is not crucial for the existence of the center of variability along 13°N, as hypothesized by CAa. This result may seem somewhat surprising at first. Westward propagation of Ekman pumping anomalies has been detected by CAa at decadal timescales, and this feature of the forcing may mainly affect the low-frequency components of the Rossby wave field. One may think that, because of the 2-yr frictional timescale used in Eq. (1), the decadal Rossby waves may be severely damped and the residual field may be only marginally influenced by the westward propagation of the forcing. However, even if a frictional timescale of 20 yr is used in Eq. (1), the solutions produced by the W_E and W_E^{sym} fields differ very little in amplitude, confirming that thermocline variability is rather insensitive to the propagation characteristics of the forcing.

The explanation of the above result lies in the fact that at decadal timescales the wavelength of the oceanic signals is much larger than the longitude band over which W_E is coherent so that phase variations over this longitude band are very small irrespective of the direction of propagation of the forcing. This can be illustrated by considering the simple case in which the Ekman pumping oscillates at a frequency ω_f and propagates westward with a phase speed c_f within the zonal band $x_f \le x \le 0$:

$$W_E = \begin{cases} W_o e^{i\omega_f(t+x/c_f)} & x_f \le x \le 0 \\ 0 & \text{elsewhere,} \end{cases} \tag{6}$$

where $x = 0$ corresponds to the eastern edge of the forced area, and not necessarily to the eastern boundary of the basin. We only consider zonal propagation, so no y dependency is explicitly included here, and for simplicity frictional processes are neglected.

Within the forcing band, the solution is the superposition of two traveling waves, one propagating at c_f and the other propagating at the speed of the free Rossby waves c_r:

$$\eta = -\frac{W_o}{i\omega_f(1 - c_r/c_f)}[e^{i\omega_f(t+x/c_f)} - e^{i\omega_f(t+x/c_r)}]. \tag{7}$$

The two traveling wave components have the same amplitude but opposite signs to satisfy the boundary condition at $x = 0$. Equation (7) can be rewritten in the form

$$\eta = \frac{2W_o}{c_r\alpha} e^{i\omega_f[t+x/(2\tilde{c})]} \sin\left(\frac{\alpha}{2}x\right), \tag{8}$$

where

$$\alpha = \frac{\omega_f}{c_r}\left(1 - \frac{c_r}{c_f}\right) \quad \text{and} \quad \tilde{c} = \frac{c_r c_f}{c_r + c_f}. \tag{9}$$

The propagation of the forcing versus that of the free waves affects the amplitude of the resulting Rossby wave field through the factor α. If, for example, $c_r \sim c_f$, α tends to zero, and Eq. (8) becomes

$$\eta = -\frac{W_o}{c_r}|x|e^{i\omega_f[t+x/(2\tilde{c})]}. \tag{10}$$

However, if the wavelength $\lambda = 2\pi c_r/\omega_f$ is much larger than $|x_f|$, the maximum value of $|x|(\alpha/2)$ can be very small independently of the ratio c_r/c_f. For $\omega_f = 10$ yr, $c_r = 16$ cm s^{-1}, the wavelength is $\lambda \sim 50\,000$ km. The ''forcing area,'' where W_E is coherent, extends approximately between the date line and 120°W so that $|x_f| \sim 5000$ km and $(2\pi/\lambda)|x_f| \sim 0.6$.

Thus, because of the long wavelength of the Rossby waves as compared with the width of the forcing area, the amplitude of the response is not very sensitive to the westward propagation of the forcing. On the other hand, the presence in the forcing of long timescales and associated long spatial scales appears to be crucial for the existence of the centers of variability at 13°N and 10°S.

d. Are the tropical centers of variability consistent with stochastic forcing?

Frankignoul et al. (1997) have examined how much of the decadal variability in the extratropical ocean can be explained by a passive oceanic response to stochastic wind forcing. They have described the characteristics of the spectra of the first-mode baroclinic Rossby waves excited by an Ekman pumping field that is zonally uniform and white in frequency domain and have shown that the geographical variations of the spectra are in good agreement with those diagnosed from the Hamburg climate model. By taking the Fourier transform of Eq. (5) without the boundary forcing term (first term on the right-hand side) and neglecting friction ($R = 0$), the power spectrum of thermocline depth produced by a zonally uniform and temporally stochastic Ekman pumping is given by

$$|\hat{\eta}(x, \omega)|^2 = \frac{2|\hat{W}_E|^2}{\omega^2}(1 - \cos\omega\Delta t), \qquad (11)$$

where ω is the frequency, $\hat{\eta}$ and $\hat{W}_E$ are the Fourier transforms of η and W_E, respectively, and Δt is the wave transit time from the eastern boundary to point x:

$$\Delta t = \frac{|x - x_e|}{c_r}. \qquad (12)$$

Here $|\hat{W}_E|^2$ is assumed to be independent of space and frequency (white noise forcing). As described by Frankignoul et al. (1997), at frequencies higher than $\omega^*(x) = 2\pi/\Delta t$ the spectrum exhibits a ω^{-2} behavior with a modulation $(1 - \cos\omega\Delta t)$, while for frequencies lower than ω^* the spectrum tends to flatten toward a level

$$|\hat{\eta}|^2 = |\hat{W}_E|^2\frac{(x - x_e)^2}{c_r^2} \quad \text{for } \omega \ll \omega^*. \qquad (13)$$

Thus, the shape of the spectrum has a strong longitudinal dependence: the frequency ω^* decreases westward, and the low-frequency level increases quadratically with the distance from the eastern boundary. According to Frankignoul et al. (1997) the high-frequency modulation of the spectrum is likely due to the neglect of friction in their simple model and would disappear if some degree of dissipation were included.

To what extent are the Rossby wave fields from the simple model and the OGCM consistent with Frankignoul et al.'s (1997) theory of a stochastically forced ocean? The ensemble averaged spectra of W_E^{SC} at different locations (not shown) have similar energy levels at all frequencies, within the 95% confidence interval, as expected for a stochastic process white in frequency domain. The ensemble average spectra of the Rossby wave field produced by W_E^{SC} at 140°W, 13.6°N, and 180°, 13.6°N are shown in Figs. 8a and 8c, respectively. Two different longitudes are considered to illustrate the x dependence of the spectra. The spectra predicted by the theory of Frankignoul et al. (1997) at the same locations, assuming the eastern boundary of the forcing region to be at ~115°W, are also shown for comparison. Notice that the spectra from the simple model in Figs. 8a and 8c are based on seasonal anomalies, while the theoretical spectra are computed for a larger frequency range. The spectrum of the Rossby wave field excited by W_E^{SC} at 140°W is in excellent agreement with the theoretical spectrum. The agreement tends to deteriorate farther west, where the low-frequency energy level of the thermocline depth spectra forced by W_E^{SC} does not increase as rapidly as predicted by the theory of Frankignoul et al. (1997). At 180° (Fig. 8c) the spectral power at periods longer than ~3 yr is lower than the power of the theoretical spectrum. The reason for the discrepancy may be associated with an energy decrease of W_E^{SC} with decreasing longitude. Also, the presence of frictional processes in the wave model may damp the amplitude of the westward propagating Rossby waves and lead to a smaller amplitude signal away from the eastern boundary than expected from the inviscid theory of Frankignoul et al. (1997).

We will refer to the spectra of thermocline displacement produced by W_E^{SC} as the ''stochastic spectra.'' In Figs. 8b and 8d the stochastic spectra are compared with the spectra of thermocline displacement from the simple model forced by W_E, and from the OGCM, at the same locations considered in Figs. 8a and 8c. The spectra of thermocline variability excited by W_E, in both the OGCM and the simple model, are characterized by higher energy levels at low frequencies with respect to the stochastic spectra, the differences being significant at the 95% level. Thus, the results from spectral analysis are consistent with those inferred from the analysis of spatial coherencies in sections 3b and 3c, indicating that the variability in the two tropical centers cannot be simply explained in terms of a ''white'' Ekman pumping forcing. The presence of a large fraction of energy at low frequencies and long spatial scales in the forcing appears to play a very crucial role for the origin of the centers of variability at 10°S and 13°N.

4. Discussion

In section 3 we have seen that a simple first-mode Rossby wave model driven by the observed forcing can reproduce the basic characteristics of the variability exhibited by the OGCM around 10°S and 13°N. This result needs to be reconciled with the findings of CAb, who have shown that meridional excursions of the thermocline can account for a large part of the variability around 13°N. Figure 9 shows the meridional section of mean temperature at 174°W from the OGCM. Poleward of ~5°S and 10°N the thermocline deepens, with maximum slopes at approximately 10°S and 13°N. At 13°N, for example, a southward displacement of the thermocline would result in a deepening of the 15°C isotherm, which may be used as a proxy for thermocline depth, and vice versa at 10°S. Following CAb, meridional displacements of the isotherms may be quantified by mon-

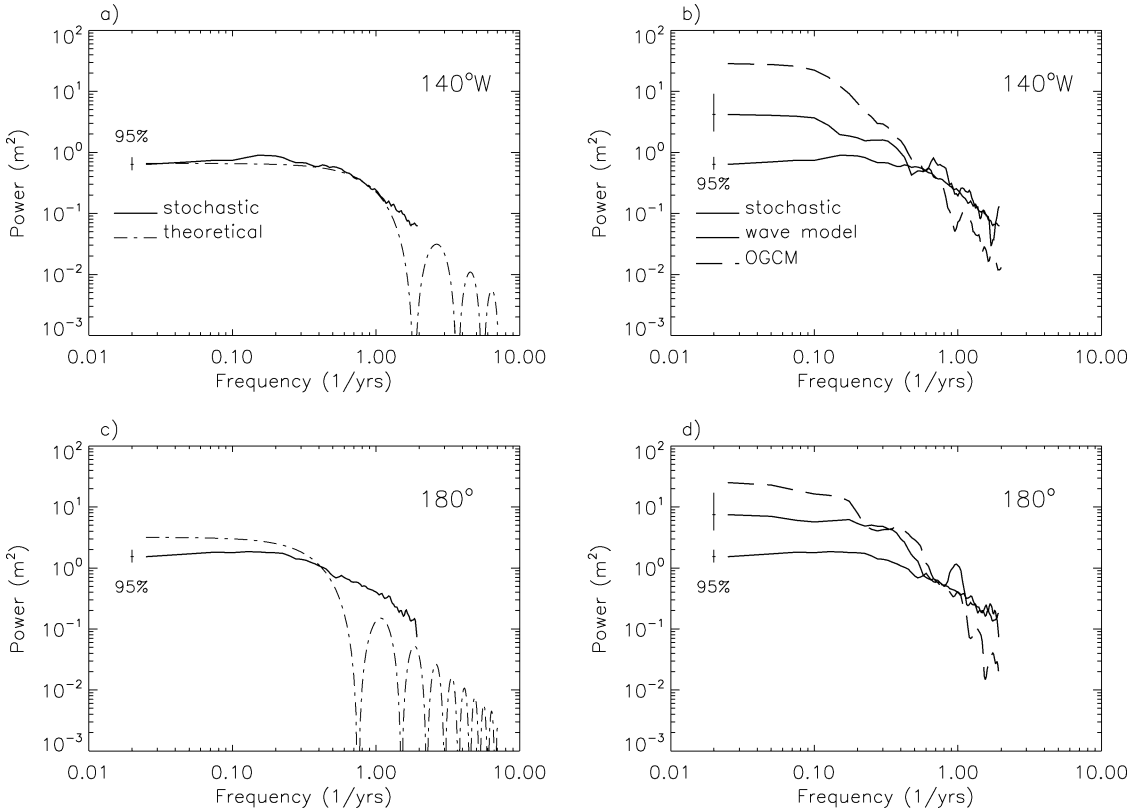

FIG. 8. (a) Ensemble average spectrum of thermocline depth variations obtained with the wave model forced by W_E^{SC} at 13.6°N, 140°W (solid line), and theoretical spectrum expected from the inviscid, first-mode baroclinic Rossby wave equation forced by a stochastic Ekman pumping white in frequency domain (dot–dash line; Frankignoul et al. 1997). (b) Comparison between the ensemble average spectrum of thermocline depth variations in (a) (solid line), the spectrum of thermocline depth variations produced by the wave equation forced with the observed W_E (dash–dot line), and the spectrum of the thermocline depth from the OGCM (dashed line) at 13.6°N, 140°W. (c) As in (a) but at 13.6°N, 180°. (d) As in (b) but at 13.6°N, 180°. The spectra from the OGCM and simple model are based on seasonal values. The 95% confidence intervals are indicated. The spectra computed as ensemble averages (with 99 elements) have a larger number of degrees of freedom.

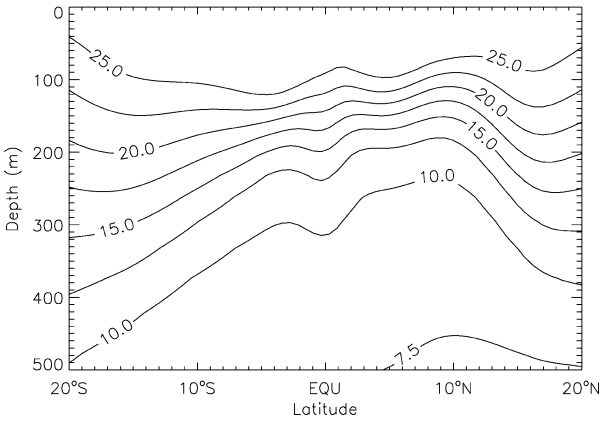

FIG. 9. Meridional section of mean temperature at 174°W. Contour interval is 2.5°C. Notice the deepening of the thermocline poleward of ~5°S and 10°N.

itoring the position of the maximum meridional slope around 13°N in the OGCM. The product of the meridional displacements around a given latitude and the slope of the thermocline at that latitude provides an estimate of the depth changes that can be expected at that location as a result of this process. The depth variations estimated with this method at 13.6°N, 186°E are compared in Fig. 10a with the depth variations diagnosed from the OGCM at the same location. The correlation coefficient between the two time series is 0.96 and the regression coefficient is 0.85. Thus, the meridional displacements detected with the above diagnostics appear to account for most of the depth changes at this location, as shown by CAb.

Rossby waves are associated with an anomalous meridional velocity v' given by

$$v' = \frac{g'}{f}\frac{\partial \eta}{\partial x}. \tag{14}$$

Thus, the Rossby wave meridional velocity is proportional to the second term in Eq. (1), the radiation

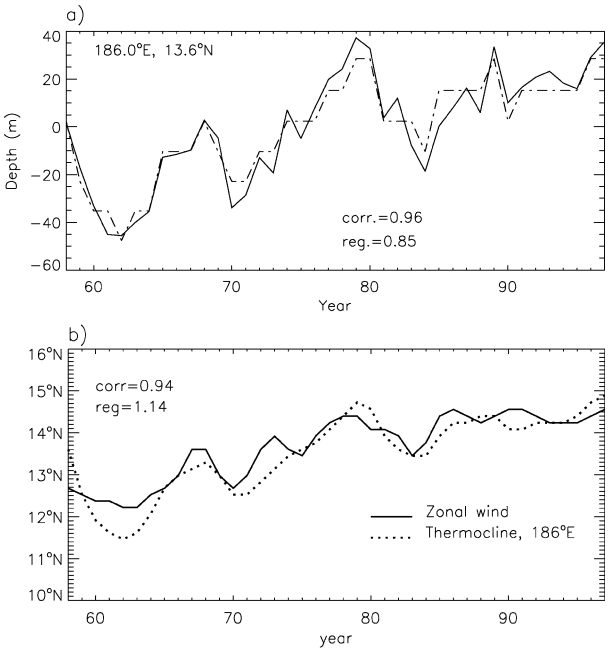

FIG. 10. (a) Comparison between the thermocline depth variations in the OGCM at 13.6°N, 174°W (solid line, m), and the thermocline depth changes inferred from the meridional excursions of the thermocline multiplied by the mean slope of the 15°C isotherm (dot–dash line). The correlation coefficient between the two time series is 0.96, and the regression coefficient is 0.85. (b) Comparison between the time evolution of the latitude at which the zonal component of the easterlies, averaged between 172°E and 140°W, achieves its maximum (solid line) and the latitudinal position of the maximum meridional slope of the thermocline around 13.6°N, 174°W (dotted line). Both estimates are based upon annually averaged data. The dotted line has been smoothed using a 3-point binomial filter.

term. In areas where the meridional slope of the mean thermocline is large, one may think that the presence of a meridional velocity field can give rise to anomalous advection of mean thermocline depth, $v'(dH/dy)$. However, in a 1½-layer, shallow-water model, like the one we are considering here, anomalous advection of mean thermocline depth is exactly cancelled by the mean zonal advection of anomalous depth, $U(\partial\eta/\partial x)$, where

$$U = -\frac{g'}{f}\frac{dH}{dy} \tag{15}$$

is the mean zonal velocity. Thus, within the dynamical framework of a 1½-layer reduced-gravity model no meridional displacement of the thermocline can be induced by the Rossby wave anomalous velocity field. Can the thermocline displacements in Fig. 10a be due to the nature of the surface forcing?

The trade winds achieve their maximum strength close to 10°S and 13°N, and since they are characterized by a large zonal scale, variations in the strength and/or position of the trade winds can plausibly be responsible for the large zonal coherency of the Ekman pumping anomalies along those latitudes. We concentrate on the Northern Hemisphere, where the maximum amplitude of the zonal wind is achieved along ~13°N, approximately between 160°E and 130°W, and focus on the zonal component of the winds. To check the possibility of meridional displacements of the trade wind system we monitor the latitude of the maximum zonal wind, averaged between 173°E and 140°W. As shown in Fig. 10b, the position of the maximum zonally averaged zonal wind does experience latitudinal variations, and these variations are largely correlated with the meridional displacements of the thermocline (diagnosed as the position of the maximum slope). The maximum correlations are achieved when the zonally averaged wind excursions lead the thermocline excursions by a lag that increases progressively westward, due to the westward propagation of the thermocline signals. At 174°W (Fig. 10b), the maximum correlation (0.94), and maximum regression (1.14) between the two time series are achieved when the zonally averaged zonal wind leads the thermocline displacement by ~1 yr. Thus, it is conceivable that the large-scale Ekman pumping anomalies along 13°N originate primarily from meridional shifts of the trade wind system.

To understand what changes in the ocean thermal structure can be induced by this type of wind variability we consider the idealized case of a purely zonal wind stress that is independent of x and varies sinusoidally with latitude over a rectangular domain with $0 < y < L_y$ as the latitudinal coordinate and $0 < x < L_x$ as the zonal coordinate. We further assume that the wind stress undergoes meridional excursions with amplitude a and frequency ω_f:

$$\tau = \tau_0 \cos\left\{\frac{2\pi}{L_y}[y - y_0(t)]\right\}, \tag{16}$$

where $y_0(t) = a\cos\omega_f t$ and $a \ll L_y$. Using trigonometric formulas and given that the amplitude a of the meridional excursions is much smaller than the latitudinal dimension of the domain, Eq. (16) can be rewritten in the form

$$\tau \cong \tau_0 \cos\left(\frac{2\pi}{L_y}y\right) + \tau_1 \sin\left(\frac{2\pi}{L_y}y\right)\cos\omega_f t, \tag{17}$$

where $\tau_1 = 2\pi\tau_0(a/L_y)$. Thus, the resulting wind stress can be expressed as the sum of a time-independent term ($\overline{\tau}$) and a time-dependent component (τ'), that also varies with latitude. The maximum mean easterlies, as expressed by $\overline{\tau}$, are achieved at $y = L_y/2$. For the analogy with the OGCM we are mainly interested in the variability around this latitude, and for simplicity we approximate the Ekman pumping as $W_E = \tau_y/(\rho_0 f)$. We further assume a zonally uniform phase speed and neglect friction. The solution of Eq. (1) with the forcing Eq. (17) is also the superposition of a time-independent component $\overline{\eta}$ forced by $\overline{\tau}$ and a time-dependent component η' forced by τ':

$$\eta(x, y, t) = \overline{\eta}(x, y) + \eta'(x, y, t), \quad (18)$$

where

$$\overline{\eta}(x, y) = H_e - \frac{2\pi\tau_0}{\rho_0 f c_r L_y}(L_x - x)\sin\left(\frac{2\pi}{L_y}y\right) \quad (19)$$

is the Sverdrup solution, H_e being the mean thermocline depth at the eastern boundary and

$$\eta'(x, y, t) = \frac{2\pi\tau_1}{\rho_0 f \omega_f L_y}\cos\left(\frac{2\pi}{L_y}y\right) \times \left\{\sin\omega_f t - \sin\left[\omega_f\left(t - \frac{x}{c_r}\right)\right]\right\}. \quad (20)$$

In order to satisfy the boundary condition of no-normal flow at the eastern boundary, H_e must be independent of y and η' must vanish at the eastern boundary: η' is the superposition of a standing wave component, which oscillates at the frequency of the forcing, and a traveling wave component with the same frequency, which propagates westward at the phase speed c_r of the free Rossby waves.

Solutions are evaluated for the domain extending from 120°E to 110°W, and spanning the latitude range between the equator and 30°N, with $a = 1.2°$, $\tau_0 = 0.4$ dyn cm^{-2}, $H_e = 100$ m, and $\omega_f = 2\pi/10$ yr. If we apply the same diagnostics used for the OGCM, by monitoring the position of the maximum slope as a function of time, we find that depth changes estimated by using the position of the maximum slope can explain most of the depth anomalies at a given point (Fig. 11a). Also, as in the OGCM, the meridional displacements of the thermocline lag the position of maximum easterlies (Fig. 11b) with a lag that increases westward (not shown).

This simple example illustrates how meridional shifts of the thermal structure, as seen in the OGCM, can result from the propagating Rossby wave field, depending on the characteristics of the forcing. Independent processes (i.e., mean or anomalous advection) are not necessarily needed to justify the occurrence of the meridional shifts of the isotherms. Also, in the analytical example above, depth anomalies only depend upon the anomalous component of the Ekman pumping, as indicated by Eq. (18) and (20), showing that the presence of the mean meridional slope does not have an enhancing effect on the thermocline variability, as may have been anticipated.

Discrepancies exist between the solution of the simple model in Eq. (1) and the OGCM. Specifically, the simple model generally underestimate the amplitude of the variability, and along 13°N thermocline variability from the simple model shows a westward intensified structure, while maximum standard deviation is found between approximately 140°E and 140°W in the OGCM (Figs. 1a, c). In particular, local maxima in thermocline variability in the OGCM, such as the one centered at ~13°N, 160°W, coincide with Ekman pumping maxima. Shorter waves not modeled by Eq. (1), which is based on the long-wave approximation, may be excited by small-scale W_E features and they may play some role in modifying the zonal structure of the variability along 13°N. Using an adjoint approach, Galanti and Tziperman (2003) have shown that low-frequency, short zonal scale baroclinic Rossby waves may be amplified along latitudes very close to the ones considered here (~12°S and 15°N) by baroclinic instability processes associated with the large climatological meridional temperature gradients. Thus, low-frequency short waves may play an important role in explaining the fraction of variance (and its zonal distribution) not accounted for by the wave model considered here. There is also the possibility that higher-mode Rossby waves are present, and may give rise to anomalous advection of mean thermocline depth, so that the presence of a sloping thermocline could influence the zonal distribution of variance. Further analyses are needed to elucidate this point.

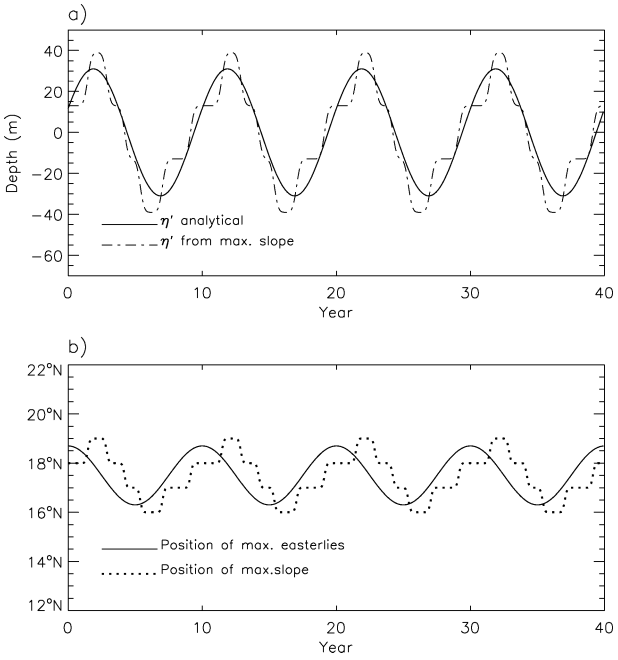

FIG. 11. Results from the idealized case of a shallow-water model forced by a zonal wind stress that undergoes meridional excursions with a frequency $\omega_f = 2\pi/10$ yr. (a) Variations of thermocline depth at 17°N, 180° (latitude of the mean maximum slope) computed from Eq. (20) (solid line) and estimated by multiplying the meridional displacements of the maximum thermocline slope by the mean slope at 17°N, 180° (dot–dash line). (b) Meridional excursions of the zonal wind stress (solid line) and evolution of the latitude of the maximum thermocline slope at 180° (dotted line).

5. Summary

In this paper we have systematically examined the relative influence of surface wind forcing and mean thermocline topography in producing centers of thermocline variability at ~10°S and 13°N. We have found that the surface Ekman pumping alone can excite centers of var-

iability around 10°S and 13°N. The aspect of the surface forcing that appears to play the dominant role in producing enhanced Rossby wave amplitudes is the spatial coherency of the Ekman pumping at those latitudes. Along each latitude, the Rossby wave field generated at any given longitude is the superposition of the westward propagating signals generated by the forcing to the east of that longitude. A surface forcing that is coherent over a large distance may excite signals that superimpose constructively, thus resulting in a larger amplitude thermocline response. Spatial coherencies increase at low frequencies, indicating that larger spatial scales are associated with longer timescales. As a result, the low-frequency components of the forcing appear to be the most effective in exciting Rossby waves at 10°S and 13°N. Despite the large decrease in the variance of the forcing when timescales shorter than 6 yr are filtered out, the maxima in thermocline variability at those latitudes remain relatively large.

The spatiotemporal structure of the Ekman pumping that emerges from the present analysis differs from that hypothesized in the theory of Frankignoul et al. (1997), where the Ekman pumping is assumed to be uniform across the basin independently of frequency. Since the ocean responds preferentially to those components of the forcing with larger spatial scales, the association of larger zonal coherencies with low-frequencies results in a ''dynamical low-pass filtering'' of the forcing. As a result, the spectra of thermocline depth at 10°S and 13°N differ from the theoretical spectra computed by Frankignoul et al. (1997) and show a systematically larger energy level at low frequencies.

The large spatial coherency of the forcing along 10°S and 13°N appears to be the fundamental factor responsible for the centers of thermocline variability along those latitudes. Local maxima in the amplitude of the forcing cannot explain the origin of the variability maxima along 10°S and 13°N but can affect their amplitude and sharpness, especially at lower frequencies.

Along 13°N Ekman pumping anomalies exhibit a westward propagation with a phase speed comparable to the phase speed of the free waves, and Capotondi and Alexander (2001a) suggested that this quasi-resonance could be responsible for the large thermocline variability around 13°N. By forcing the wave model with an Ekman pumping field with modified propagation characteristics we find that quasi-resonance does not significantly influence the amplitude of the thermocline variability. Because of the long wavelength of the waves in comparison with the longitude range of the propagating Ekman pumping anomalies, the phase variations of the forcing are too small to significantly affect the waves.

Along 10°S and 13°N the mean thermocline deepens poleward, with large meridional gradients of thermocline depth, and so one may speculate that meridional excursions of the thermocline, associated with anomalous advection of mean thermocline depth, may be responsible for a large fraction of thermocline variability along those latitudes. Capotondi and Alexander (2001b) show that the location of the maximum meridional gradients of thermocline depth around 13°N does exhibit meridional excursions whose magnitude could account for most of the thermocline variability along 13°N. However, advection of mean thermocline topography by the anomalous meridional velocities associated with the wave field is exactly cancelled by the zonal advection of thermocline depth anomalies by the mean flow. Meridional shifts of the trade wind system may be responsible for the large zonal coherency of the Ekman pumping along 10°S and 13°N. Using an idealized example, in which a purely zonal wind stress undergoes small-amplitude meridional excursions, we illustrated how this type of wind variability may produce meridional displacements of the thermocline similar to those seen in the NCAR OGCM as a result of the propagating Rossby wave field, without the inclusion of advection processes.

It is not clear whether the wind variability along 10°S and 13°N results from the atmospheric response to sea surface temperature anomalies in the equatorial band or in midlatitudes or is due to internal atmospheric processes. Another open question concerns the existence of possible atmospheric feedbacks to sea surface temperature anomalies associated with the Rossby wave field. These issues cannot be properly addressed in the context of a hindcast simulation as the one analyzed here, but need to be examined using observations or coupled model simulations.

Acknowledgments. We thank the NCAR Oceanography Section for making the model output available to us, and for useful discussions. We also thank the two anonymous reviewers, who have provided very insightful and constructive comments. This work was supported by NOAA-GOALS Grant GC98-139, and by an omnibus grant from the NOAA Office of Global Programs to the Climate Diagnostics Center.

REFERENCES

Capotondi, A., and M. A. Alexander, 2001a: Rossby waves in the tropical North Pacific and their role in decadal thermocline variability. *J. Phys. Oceanogr.*, **31,** 3496–3515.

——, and ——, 2001b: The influence of thermocline topography on the oceanic response to fluctuating winds: A case study in the tropical North Pacific. *Advances in Mathematical Modeling of Atmosphere and Ocean Dynamics*, P. F. Hodnett, Ed., Kluwer, 119–124.

Cessi, P., 2000: Thermal feedback on wind stress as a contributing cause of climate variability. *J. Climate*, **13,** 232–244.

Deser, C., M. A. Alexander, and M. S. Timlin, 1996: Upper-ocean thermal variations in the North Pacific during 1970–1991. *J. Climate*, **9,** 1840–1855.

Doney, S. C., S. Yeager, G. Danabasoglu, W. G. Large, and J. C. McWilliams, 2003: Modeling global oceanic interannual variability (1958–1997): Simulation design and model-data evaluation. NCAR Tech. Note NCAR/TN-452+STR.

Frankignoul, C., P. Müller, and E. Zorita, 1997: A simple model of

the decadal response of the ocean to stochastic wind forcing. *J. Phys. Oceanogr.,* **27,** 1533–1546.
Galanti, E., and E. Tziperman, 2003: A midlatitude–ENSO teleconnection mechanism via baroclinically unstable long Rossby waves. *J. Phys. Oceanogr.,* **33,** 1877–1888.
Gent, P. R., and J. C. McWilliams, 1990: Isopycnal mixing in ocean circulation models. *J. Phys. Oceanogr.,* **20,** 150–155.
——, F. O. Bryan, G. Danabasoglu, S. C. Doney, W. R. Holland, W. G. Large, and J. C. McWilliams, 1998: The NCAR Climate System Model global ocean component. *J. Climate,* **11,** 1287–1306.
Grötzner, A., M. Latif, and T. P. Barnett, 1998: A decadal climate cycle in the North Atlantic ocean as simulated by the ECHO coupled GCM. *J. Climate,* **11,** 831–847.
Gu, D., and S. G. H. Philander, 1997: Interdecadal climate fluctuations that depend on exchanges between the tropics and extratropics. *Science,* **240,** 1293–1302.
Haney, R. L., 1971: Surface thermal boundary condition for ocean circulation models. *J. Phys. Oceanogr.,* **1,** 241–248.
Jin, F.-F., 1997: A theory of interdecadal climate variability of the North Pacific ocean–atmosphere system. *J. Climate,* **10,** 324–338.
Kalnay, E., and Coauthors, 1996: The NCEP/NCAR 40-Year Reanalysis Project. *Bull. Amer. Meteor. Soc.,* **77,** 437–471.
Kessler, W. S., 1990: Observations of long Rossby waves in the northern tropical Pacific. *J. Geophys. Res.,* **95,** 5183–5217.
Large, W. G., and S. Pond, 1982: Sensible and latent heat flux measurements over the ocean. *J. Phys. Oceanogr.,* **12,** 464–482.
——, J. C. McWilliams, and S. C. Doney, 1994: Oceanic vertical mixing: A review and a model with a nonlocal boundary layer parameterization. *Rev. Geophys.,* **32,** 363–403.
——, G. Danabasoglu, and S. C. Doney, 1997: Sensitivity to surface forcing and boundary-layer mixing in a global ocean model: Annual mean climatology. *J. Phys. Oceanogr.,* **27,** 2418–2447.
——,——, J. C. McWilliams, P. R. Gent, and F. O. Bryan, 2001: Equatorial circulation of a global ocean climate model with anisotropic horizontal viscosity. *J. Phys. Oceanogr.,* **31,** 518–536.
Latif, M., and T. P. Barnett, 1994: Causes of decadal climate variability over the North Pacific and North America. *Science,* **266,** 634–637.
——, and ——, 1996: Decadal climate variability over the North Pacific and North America: Dynamics and predictability. *J. Climate,* **9,** 2407–2423.
Lysne, J., and C. Deser, 2002: Wind-driven thermocline variability in the Pacific: A model–data comparison. *J. Climate,* **15,** 829–845.
Matsumoto, M., and T. Nishimura, 1998: Mersenne Twister: A 623-dimensionally equidistributed uniform pseudorandom number generator. *ACM Trans. Model. Comput. Simul.,* **8,** 3–30.
Morse, P. M., and H. Feshbach, 1953: *Methods of Theoretical Physics.* McGraw-Hill, 997 pp.
Münnich, M., M. Latif, S. Venzke, and E. Maier-Reimer, 1998: Decadal oscillations in a simple coupled model. *J. Climate,* **11,** 3309–3319.
Neelin, J. D., and W. Weng, 1999: Analytical prototypes for ocean–atmosphere interaction at midlatitudes. Part I: Coupled feedbacks as a sea surface temperature dependent stochastic process. *J. Climate,* **12,** 697–721.
Qiu, B., W. Miao, and P. Müller, 1997: Propagation and decay of forced and free baroclinic Rossby waves in off-equatorial oceans. *J. Phys. Oceanogr.,* **27,** 2405–2417.
Robertson, A. W., 1996: Interdecadal variability over the North Pacific in a multicentury climate simulation. *Climate Dyn.,* **12,** 227–241.
Schneider, N., A. J. Miller, M. A. Alexander, and C. Deser, 1999: Subduction of decadal North Pacific temperature anomalies: Observations and dynamics. *J. Phys. Oceanogr.,* **29,** 1056–1070.
Talley, L., 1999: Simple coupled midlatitude climate models. *J. Phys. Oceanogr.,* **29,** 2016–2037.
Watanabe, M., and M. Kimoto, 2000: Behavior of midlatitude decadal oscillations in a simple atmosphere–ocean system. *J. Meteor. Soc. Japan,* **78,** 441–460.
White, W. B., 1977: Secular variability in the baroclinic structure of the interior North Pacific from 1950–1970. *J. Mar. Res.,* **35,** 587–607.
Wyrtki, K., 1975: Fluctuations of the dynamic topography in the Pacific Ocean. *J. Phys. Oceanogr.,* **5,** 450–459.
Xu, W., T. P. Barnett, and M. Latif, 1998: Decadal variability in the North Pacific as simulated by a hybrid coupled model. *J. Climate,* **11,** 858–870.